

Curvelet analysis of asteroseismic data

I: Method description and application to simulated sun-like stars

P. Lambert^{1,2}, S. Pires^{3,1}, J. Ballot^{2,4}, R. A. García^{1,2}, J.-L. Starck^{3,1} and S. Turck-Chièze^{1,2}

¹ DSM/DAPNIA/Service d'Astrophysique, CEA/Saclay, 91191 Gif-sur-Yvette Cedex, France
e-mail: lambertp@cea.fr

² AIM – Unité Mixte de Recherche CEA - CNRS - Université Paris VII – UMR n°7158, CEA/Saclay, 91191 Gif-sur-Yvette Cedex, France

³ DSM/DAPNIA/Service d'Electronique des Détecteurs et d'Informatique, CEA/Saclay, 91191 Gif-sur-Yvette Cedex, France

⁴ Max-Planck-Institut für Astrophysik, Karl-Schwarzschild-Str. 1, Postfach 1317, 85741 Garching, Germany

Received 2005 November 18; Accepted 2006 March 31

ABSTRACT

Context. The detection and identification of oscillation modes (in terms of their ℓ , m and successive n) is a great challenge for present and future asteroseismic space missions. The “peak tagging” is an important step in the analysis of these data to provide estimations of stellar oscillation mode parameters, i.e., frequencies, rotation rates, and further studies on the stellar structure.

Aims. To increase the signal-to-noise ratio of the asteroseismic spectra computed from time series representative of MOST and CoRoT observations (30- and 150-day observations).

Methods. We apply the curvelet transform – a recent image processing technique which looks for curved patterns – to echelle diagrams built using asteroseismic power spectra. In this diagram the eigenfrequencies appear as smooth continuous ridges. To test the method we use Monte Carlo simulations of several sun-like stars with different combinations of rotation rates, rotation-axis inclination and signal-to-noise ratios.

Results. The filtered diagrams enhance the contrast between the ridges of the modes and the background allowing a better tagging of the modes and a better extraction of some stellar parameters. Monte Carlo simulations have also shown that the region where modes can be detected is enlarged at lower and higher frequencies compared to the raw spectra. Even more, the extraction of the mean rotational splitting from modes at low frequency can be done more easily than using the raw spectrum.

Key words. Stars: oscillations – Methods: data analysis – Techniques: image processing

1. Introduction

Helioseismology – the study of solar oscillations – is a powerful probe of the structure and dynamics of the Sun which has provided great improvements in our understanding of stellar evolution and structure (Turck-Chièze et al. 1993; Christensen-Dalsgaard 2002, and references therein). Those successes push the community to apply seismic techniques to other stars, opening the doors to asteroseismology, the study of stellar oscillations. These oscillations have already been observed from ground and space. The ground-based observations are limited by the day-night cycle, which introduces aliases in the observations, but allow to use Doppler velocity measurements. They have provided data with sufficient quality to detect solar-like oscillations (see Bouchy & Carrier 2003; Bedding & Kjeldsen 2003, and references therein). To reduce the aliases, multi-site campaigns have been carried out but they are too short to have a good frequency resolution. Space pho-

tometry missions and ground-based velocity networks must be used to provide observations of stellar oscillations without these limitations. With the current MOST¹ and WIRE² satellites and the future COROT³ mission asteroseismology is blooming. However, we still have to deal – in the case of solar-like oscillations – with very small signal-to-noise ratio (hereafter S/N) observations as a consequence of the weakness of the luminosity variations. Moreover, stars cannot be spatially resolved yet. Only global oscillation modes can be observed. In addition, we cannot have access to the rotation rates and the rotation-axis inclination separately. Without knowing these two key stellar properties, the tagging of the modes in terms of their properties (ℓ, m) and successive n may be extremely difficult. In fact, the main problem to face will not be to fit the peaks (“peak-bagging”) but to provide a good description

¹ Microvariability and Oscillations of STars (Matthews 1998)

² Wide-field Infra Red Explorer (Buzasi et al. 2000)

³ Convection Rotation and planetary Transits (Baglin et al. 2001)

of the model to be fitted after having put the correct labels on the modes (“peak tagging”). To do this, it has been proposed to use the echelle diagram where the modes follow ridges depending on the stellar properties. To improve the S/N ratio Bedding et al. (2004) proposed to filter this diagram by a vertical smoothing. However the smoothing works well only when the ridges are quasi-vertical which means a very good *a priori* knowledge of the large difference and is restricted to the asymptotic part of the spectrum. We propose here to follow a similar approach but using new mathematical denoising techniques better suited to the study of curved ridges.

At the end of the last decade, the application of mathematical transforms based on wavelets to analyze astronomical images has been widely developed. The first wavelet algorithms were well adapted to treat images with isotropic elements. However, this description presented a limitation in the context of astrophysics, where objects such as filaments or spiral structures exhibit a highly anisotropic character (in shape and scale). New transforms, the ridgelet (Candès 1998) and curvelet transforms (Candès & Donoho 1999; Starck et al. 2002), were then developed to deal efficiently with such objects. Astrophysical applications (image denoising) of this technique have been presented in Starck et al. (2003, 2004) to analyze images of gravitational arcs, the Saturn rings or the CMB (Cosmic Microwave Background) map.

In this paper we suggest to use the curvelet transform to analyze asteroseismic observations (more precisely the stellar echelle diagrams), in order to improve the “peak tagging” of the oscillation modes and even the resultant “peak bagging”. To illustrate the application of this denoising technique in the asteroseismic case, we have performed Monte Carlo simulations of ideal asteroseismic data contaminated by different levels of stochastic noise. We start in Sect. 2 by a quick reminder of the properties of stellar oscillation modes in the solar-like case and the construction of the echelle diagram. In Sect. 3 we introduce multiscale transforms, in particular the ridgelet and the curvelet transforms. In Sect. 4, the simulated data of a star with an oscillation spectrum similar to the Sun but with different rotation axis inclinations and rotation rates, are presented. In Sect. 5 we discuss the results obtained in the simulations.

2. Properties of solar-like oscillations

Only low-degree stellar oscillation modes can be detected and observed with the present generation of instruments. The asymptotic theory of oscillation modes ($n \gg \ell$) is then adequate and can be used to study them. First order (Tassoul 1980) and second order developments (Vorontsov 1991; Lopes & Turck-Chièze 1994; Roxburgh & Vorontsov 2000a,b) have been made to describe solar and stellar oscillations. In the case of solar-like stars, where p-modes predominate, the frequencies can be developed as:

$$\nu_{n,\ell} \approx \Delta\nu_0 \left(n + \frac{\ell}{2} + \frac{1}{4} + \alpha(\nu) \right) + \frac{\Delta\nu_0}{4\pi^2\nu_{n,\ell}} \left((\ell + 1/2)^2 A + \psi \right) \quad (1)$$

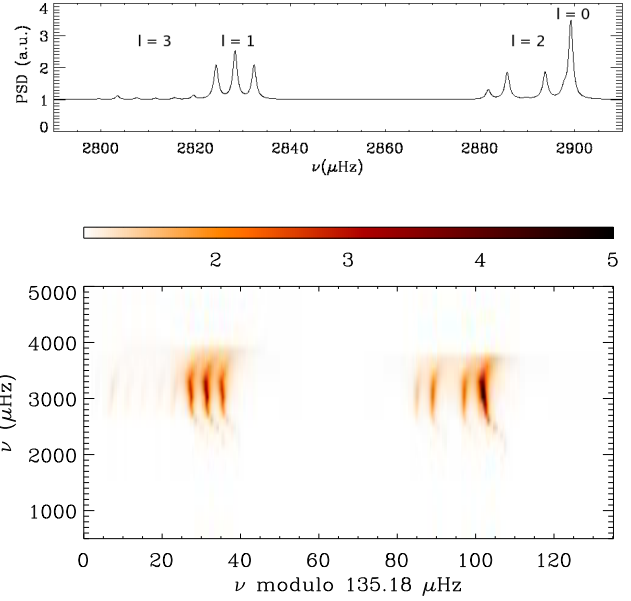


Fig. 1. Portion of the theoretical spectrum (top) and echelle diagram (bottom) for a sun spinning ten times faster than the Sun and seen under an angle of 50° . This is the ideal power spectrum used in the simulations described in Sect. 5.

in this expression ℓ and n are respectively the degree and the radial order of the modes and

$$\tau_c = \int_{r_{in}}^{r_{out}} \frac{dr}{c_s}$$

$$\Delta\nu_0 = \frac{1}{2\tau_c}$$

$$A = \frac{1}{4\pi^2\nu_{n,\ell}} \left(\frac{c_s(R_\star)}{R_\star} - \int_{r_{in}}^{r_{out}} \frac{dc_s}{dr} \frac{dr}{r} \right)$$

c_s is the internal stellar sound speed, α is a phase-shift term and ψ is a function which allows to take into account the gravitational potential in the central region (Lopes & Turck-Chièze 1994). From the asymptotic approach, we can extract general properties of modes and better understand the physics hidden in the frequencies behavior. The large frequency spacing, defined as $\Delta\nu_{n,\ell} = \nu_{n+1,\ell} - \nu_{n,\ell}$, tends asymptotically to $\Delta\nu_0$, related to the mass and radius of the star; the small frequency spacing, $\delta_{\ell,\ell+2}\nu = \nu_{n,\ell} - \nu_{n-1,\ell+2}$, can be approximated to first order by $(4\ell + 6)\Delta\nu_0 / (4\pi^2\nu_{n,\ell}) \int_0^{R_\star} \frac{dc_s}{dr} \frac{dr}{r}$. This variable is related to the derivative of the sound speed and enhances the effect coming from the central regions, providing constraints on the age of the star. Finally the second difference is defined as $\delta_2\nu = \nu_{n+1,\ell} - 2\nu_{n,\ell} + \nu_{n-1,\ell}$. Its variations provide information about the extent of the convective zone (Monteiro et al. 2000; Ballot et al. 2004b) or the helium abundance in the stellar envelope (Basu et al. 2004).

Under the rotation effects the azimuthal order m ($-\ell \leq m \leq \ell$) is needed to characterize the oscillation spectrum. If the angular velocity Ω is uniform (Ledoux 1951), the mode frequencies are asymptotically approximated by:

$$\nu_{n,\ell,m} \approx \nu_{n,\ell} + m\Omega/2\pi = \nu_{n,\ell} + m\delta\nu \quad (2)$$

where $\delta\nu$ is the rotational splitting. Equation 2 shows that modes are $(2\ell + 1)$ -times degenerated among the azimuthal order: a single peak in the spectrum becomes a multiplet. Its corresponding structure depends on the rotation rate, the inclination axis of the star and its stochastic excitation. The solar-like mode lifetimes (a few days) are expected to be much shorter than the length of the future space observations (a few months). In consequence, the relative amplitude ratios inside a multiplet will only depend, in average, on the inclination angle and the spacing between these different m -components (Gizon & Solanki 2003). Thus if the different m -components of a multiplet can be identified and tagged with the correct (ℓ, m) , they can provide a good estimation of both the rotation-axis inclination i and the rotational splitting $\delta\nu$, allowing a better mode parameter extraction through the fitting of the spectra. The effect of the stochastic excitation on an isolated mode could be minimized by computing the average of these parameters on several modes (see for example the n -collapsogramme; Ballot et al. 2004a).

Equation 1 shows that the even ($\ell = 0, 2$) and odd ($\ell = 1, 3$) modes have respectively almost the same frequency, only separated by the small spacing $\delta_{\ell, \ell+2}\nu$. In addition, they are separated regularly in frequency by the large spacing $\Delta\nu_{n, \ell}$. This property allows us to build the so-called echelle diagram (Grec et al. 1983), which is currently used to identify modes for solar-like oscillations. It is a 2D representation of the power spectrum where this one is folded onto itself in units of the large spacing. In such representation the modes appear as almost locally vertical ridges (see Fig. 1). The echelle diagram is a powerful tool for the “peak tagging” since assigning the correct (ℓ, m) values to the peaks is easier when the multiplet structure is well identified in this diagram. The successive n values are obtained from each individual horizontal line.

3. Multiscale Transforms

3.1. The Wavelet Transform

The wavelet transform provides a framework for decomposing images into their elementary constituents across scales by reducing the number of significant coefficients necessary to represent an image. The continuous wavelet transform of a 2D signal is defined as:

$$W(a, b_i, b_j) = \frac{1}{\sqrt{a}} \iint f(x, y) \psi^* \left(\frac{x - b_i}{a}, \frac{y - b_j}{a} \right) dx dy \quad (3)$$

where $W(a, b)$ are the wavelet coefficients of the function $f(x, y)$, $\psi(x)^*$ is the conjugate of the analyzing wavelet, $a > 0$ is the scale parameter and b is the position parameter. The continuous wavelet transform is the sum over all the positions of the signal $f(x, y)$ multiplied by the scaled and shifted versions of the wavelet $\psi((x - b_i)/a, (y - b_j)/a)$ (cf. Fig. 2, top panels). This process produces wavelet coefficients that are a function of scale and position.

However, the classical wavelet transform only address a portion of the whole range of interesting phenomena: isotropic features at all scales and locations. One of the drawbacks of the

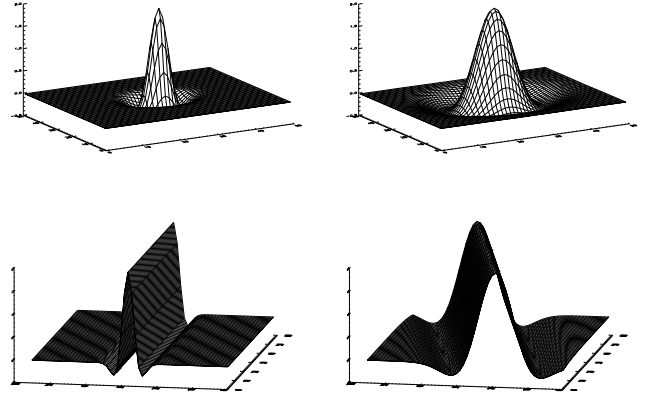


Fig. 2. Examples of 2D wavelets (top panels) and ridgelets (bottom panels). The top right wavelet has a greater scale parameter than this on the left. The bottom right ridgelet has different orientation and width than the left one.

two-dimensional wavelet transform is that it does not achieve an efficient analysis of images which present high anisotropy. For instance, the wavelet transform does not efficiently approximate 2D edges, since a large number of large wavelet coefficients, scale after scale, are required, making difficult its analysis. In order to solve this problem two new mathematical transforms, namely the ridgelet transform and the curvelet transform, were introduced.

3.2. The Ridgelet transform

The ridgelet transform was developed to process images including ridges elements (Candès 1998). It provides a representation of perfectly straight edges. Given a function $f(x_1, x_2)$, the representation of this latter is the superposition of elements of the form $a^{-1/2}\psi((x_1 \cos \theta + x_2 \sin \theta - b)/a)$, where ψ is a wavelet, $a > 0$ a scale parameter, b a location parameter and θ an orientation parameter. The ridgelet is constant along lines $x_1 \cos \theta + x_2 \sin \theta = \text{const}$, and transverse to these ridges it is a wavelet. Thus, contrary to a unique wavelet transform, the ridgelet has two supplementary characteristics: a length, equal to this of the image and an orientation, allowing the analysis of an image in every direction and so exhibiting the edge structure. Fig. 2 (bottom panels) shows two examples of ridgelets. The problem is that in the nature edges are typically curved rather than straight so ridgelets alone cannot yield an efficient representation.

3.3. The Curvelet transform

3.3.1. Description

Ridgelets can be adapted to represent objects with curved edges using an appropriate multiscale localization: at a sufficiently fine scale a curved edges can be considered as almost straight. Candès & Donoho (1999) developed the curvelet transform us-

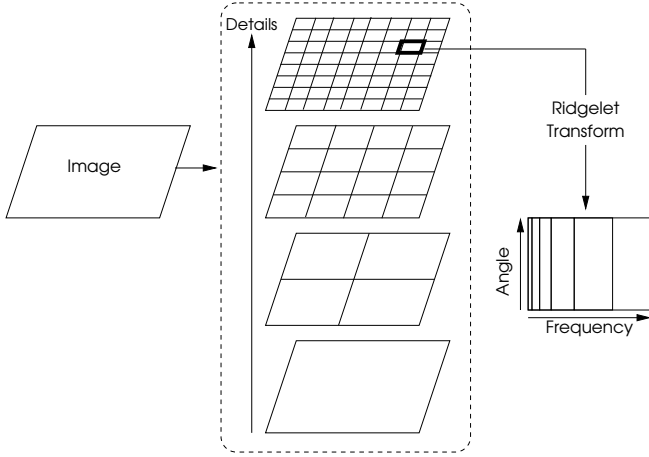


Fig. 3. Sketch illustrating the curvelet transform applied to an image. The image is decomposed into subbands followed by a spatial partitioning of each subband. The ridgelet transform is applied to each block. The finest details correspond to the highest frequencies.

ing ridgelets in this localized manner. Fig. 3 shows the different steps of the curvelet analysis of an image:

1. Image decomposition into subbands: as a set of wavelets bands through a 2D isotropic wavelet transform. Each band corresponds to a different scale.
2. Smooth partitioning: each subband is partitioned into squares – blocks –, whose size is appropriate to each scale. The finest is the scale, the smaller are the blocks.
3. Ridgelet analysis: it's applied to each square.

The implementation of the curvelet transform offers an exact reconstruction and a low computational complexity. Like ridgelets, curvelets occur at all scales, locations and orientations. Moreover contrary to ridgelets, which have a given length (the image size) and a variable width, the curvelets have also a variable length (the block size) and consequently a variable anisotropy. The finest the scale is, the more sensitive to the curvature the analysis is. As a consequence, curved singularities can be well approximated with very few coefficients.

3.3.2. Denoising images: filtering curvelet coefficients

To remove noise a simple thresholding of the curvelet coefficients has been applied to select only significant coefficients. One possible thresholding of a noisy image consists in setting to 0 all non-significant curvelet coefficients $\tilde{c}_{i,j,l}$, i , j and l respectively the indexes of the line, row and scale: it is the so-called hard-thresholding:

$$\tilde{c}_{i,j,l} = \begin{cases} 1 & \text{if } c_{i,j,l} \text{ is significant} \\ 0 & \text{if } c_{i,j,l} \text{ is not significant} \end{cases} \quad (4)$$

Commonly, $c_{i,j,l}$ is significant if the probability that the curvelet coefficient is due to noise is small, i.e., if the curvelet coefficient is greater than a given threshold. A basic problem remains: the choice of the threshold. Usually, this threshold is taken equal

to $k\sigma_j$, where σ_j is the noise standard deviation at the scale j and k is a constant taken equal to 5 in our filterings.

Simple thresholding of the curvelet coefficients is very competitive (Starck et al. 2002) with “state of the art” techniques based on wavelets, including thresholding of decimated or undecimated wavelet transforms.

4. Simulation of data

To characterize the curvelet denoising technique applied to the asteroseismic data, we have simulated typical solar-like observations varying different parameters: S/N ratios, observational lengths, rotation-axis inclinations, rotation rates... With this approach we know the input parameters in advance and we can evaluate the quality of the results given by the curvelet analysis and its limits.

In the simulations shown in this paper, we use the oscillation spectrum of a star similar to the Sun but seen under different conditions. Different rotation-axis inclinations ($i = 50^\circ$ and 90°) and rotation rates ($\Omega = \Omega_\odot$, $5\Omega_\odot$, and $10\Omega_\odot$) have been considered. An ideal power spectrum were constructed first. Only the modes $\ell \leq 3$, $n = 12-25$ were simulated. The mode parameters – frequencies (ν), amplitudes (A) and widths (Γ) – were obtained from the analysis of GOLF (Global Oscillations at Low Frequency) data (García et al. 2004). The amplitudes were corrected to take into account the difference between intensity and velocity observations. Modes were simulated with symmetrical Lorentzian profiles as the asymmetry is expected to be at the level of the noise. Following the method described in Fierry Fraillon et al. (1998), a multiplicative noise, a χ^2 with 2 d.o.f. statistics, has been introduced to reproduce the stochastic excitation of such modes (see also Anderson et al. 1990). The S/N ratio of the “resultant” raw power spectrum was defined as the maximum of the bell-shaped p-mode power (i.e. the highest simulated p mode) divided by the noise dispersion. The simulated background is flat assuming that it has been previously fitted and removed as it is usually done for the Sun (Harvey 1985).

Several Monte Carlo simulations have been performed for each ideal spectrum. Realistic S/N , with values ranging from 5 to 15, have been used to cover a wide range of situations (compatible with what it is expected, (see Baglin et al. 2001)). In each realization of the Monte Carlo simulation the same level of noise has been randomly added to the corresponding ideal spectra. Therefore all the realizations, in a given Monte Carlo simulation, have the same S/N ratio. The simulated spectra have been computed for two resolutions, ≈ 0.38 and $\approx 0.077 \mu\text{Hz}$, corresponding respectively to 30-day and 150-day observations. The first are representative of MOST observations and the short CoRoT runs while the latter are of the same length than the long CoRoT runs.

Simulations of other stars, like some potential main CoRoT targets, with different masses, ages and, in consequence, internal structures have been made. The results have already been presented and discussed during the CoRoT workshops #8 and #9 obtaining the same qualitative results. For the sake of clarity, they are not shown here.

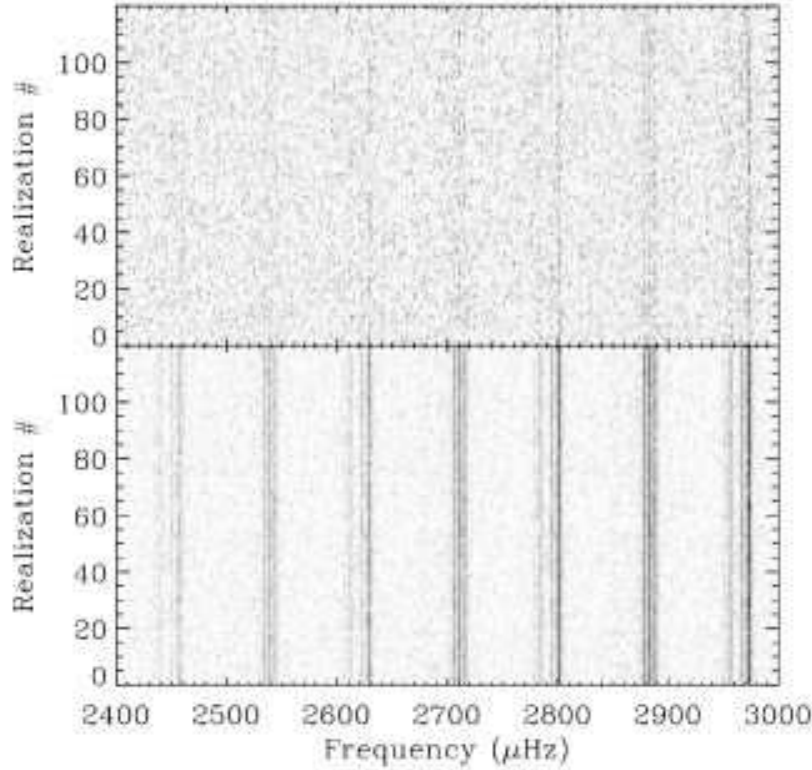


Fig. 4. Effect of the curvelet denoising on the mode visibility for $S/N = 5$. Each picture shows 120 realizations out of the 500 done in our Monte Carlo simulation. Each horizontal line corresponds to a single realization. The top panel is the raw spectra and the bottom is the curvelet filtered one.

5. Discussion

Once the spectra have been computed, the echelle diagrams can be built with a fixed folding frequency. This one corresponds to the mean large frequency spacing $\Delta\nu_0$, identified either by computing the FFT, the autocorrelation of the spectra or any other technique (see for example Régulo & Roca Cortés 2002). The denoising based on the curvelet transform is then applied to this echelle diagrams. It is important to note that artifacts may appear in the filtered spectra at frequencies $\nu^* = \nu_0 + k\Delta\nu_0$, with k an integer, when random small structures appear in the echelle diagrams. However, their appearance and position strongly depend on the folding frequency and are very sensitive to its value. Therefore they can be easily identified. The artifacts can be reduced (in contrast to the regions containing signal) by building echelle diagrams with slightly different folding frequencies and averaging the resultant filtered spectra.

In order to present the results of data analysis using the curvelet denoising method, we have selected the case of a sun-like star seen with an inclination angle $i = 50^\circ$ and with a rotation $\Omega = 10\Omega_\odot$. A portion of the ideal spectra constructed for this star can be seen in Fig. 1 (top panel). Monte Carlo simulations were then performed, giving rise to different sets (each one with 500 realizations) of raw spectra with different S/N ratios. The echelle diagrams were constructed using a folding frequency of $135.18 \mu\text{Hz}$, obtained by computing the FFT of the raw spectrum.

5.1. Peak tagging

In those cases, with a high S/N (typically 15), the mode structure is clearly visible in each raw spectrum and also on the echelle diagram. The different ridges can be easily identified and tagged. Although the filtering gives enhanced denoised diagrams and unfolded spectra, it does not contribute significantly to the mode identification.

In the lower S/N cases, however, the situation is different. Figure 4 shows some of the results of the Monte Carlo simulation for $S/N=5$. The upper panel corresponds to 120 realizations among the 500 computed for the raw spectra in the frequency range 2450–2920 μHz . Each horizontal line corresponds to a single realization. Some patterns can hardly be seen. The lower panel represents the same spectra after applying the curvelet filtering. A series of vertical ridges clearly appears. From the left to the right on the panels, they can be identified as the $(\ell = 2; m = \pm 1)$, the $\ell = 0$ (blended with the $\ell = 2; m = +2$) and the $(\ell = 1; m = -1, 0, +1)$. The improvement of the contrast is important in all the realizations and allows to distinguish the different components of a mode, making easier the identification and the tagging.

The identification is harder when looking at each individual spectrum and requires the use of the echelle diagram. Fig. 5 shows an example of raw (left) and filtered (right) 150-day observation power spectra (top and middle panels) and the corresponding echelle diagrams (bottom panels) for a $S/N = 5$

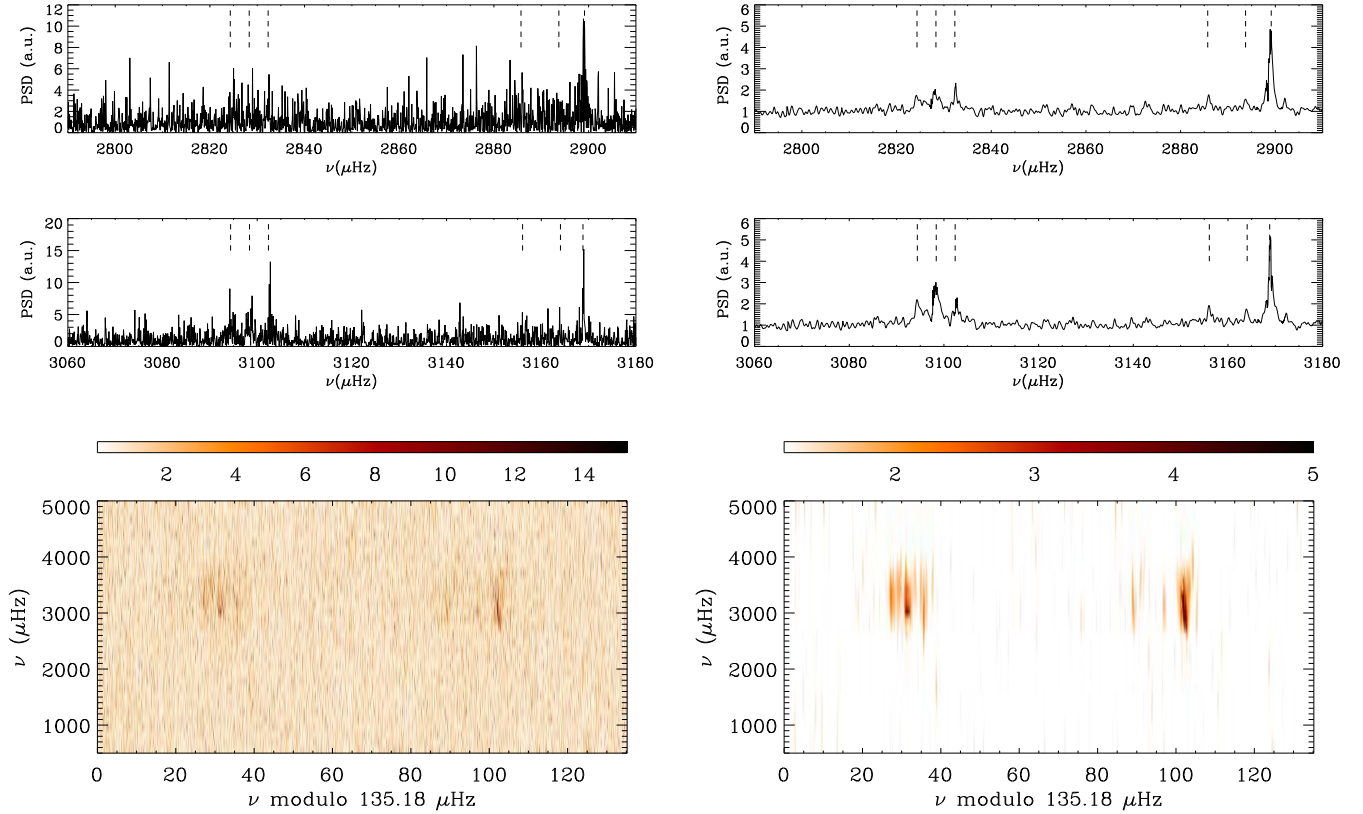


Fig. 5. Raw (left) and filtered (right) power spectra (top and middle panels) and echelle diagrams (bottom panels) for a $S/N = 5$ realization. The short dashed lines in the power spectra represent the position of the theoretical frequencies. From left to right, the three first equidistant lines indicate the components $m = -1, 0, 1$ of $\ell = 1$ modes, the two next indicate the strongest components of $\ell = 2$ ($m = -1$ and 1), and the last indicates $\ell = 0$. In this case only two components of the $\ell = 1$ and the $\ell = 0$ mode are slightly visible in the raw diagram. On the curvelet filtered one, the three $\ell = 1$ components appear as well as the $\ell = 0$ and the components $m = \pm 1$ of the $\ell = 2$ modes.

realization. Input frequencies are indicated by the short dashed lines above the spectra. The mode peaks can hardly be distinguished in the raw spectrum and can easily be confused with noise. For the range $2780\text{--}2920\text{ }\mu\text{Hz}$, only a strong peak at $2900\text{ }\mu\text{Hz}$ can be considered not to be noise. In the region $3060\text{--}3180\text{ }\mu\text{Hz}$ the peaks are visible and we can attempt to identify the $\ell=1$ and $\ell=0$ modes but it is still unclear. On the contrary, on the corresponding parts of the filtered spectrum, the structures of the $\ell=1$ mode with three components, the $\ell=0$ mode and even the strongest components of the $\ell=2$ mode are visible. The raw echelle diagram gives no extra information because of the very weak ridges and low contrast with the background. The weakest components can hardly be detected and no tagging can be done. The curvelet filtering provides a contrast enhancement of the ridges on the echelle diagram. Thus three almost equidistant strong ridges appear on the left of the diagram and one strong ridge with two weaker ones on the right. The corresponding patterns can be seen on the filtered spectrum corresponding well to the theoretical frequencies. Since the modes $\ell = 3$ are not visible, and according to the amplitude of the strongest peak on the left, we can suggest that the three strongest peaks correspond to a $\ell = 1$ multiplet and the other ones to the $\ell = 2$ and $\ell = 0$ modes.

Consequently, when the tagging is done it is also easier to have a first estimation of both the mean rotational splitting and the rotation-axis inclination, since the visibility of the multiplet is increased. From the spacing between the components of the mode $\ell = 1$, a first estimation of the mean rotational splitting of the star can be done, as well as an estimation of the inclination angle, according to their relative amplitude ratios. We have selected the extraction of one parameter: the mean rotational splitting of the $\ell=1$ mode at low frequency ($2540\text{--}2550\text{ }\mu\text{Hz}$), to quantify the improvement of the curvelet filtering. This region is particularly interesting because the line width is still small and the modes, when they are visible, can be easily identified. Thus, in a sample of 100 realizations of the Monte Carlo simulation, we have obtained in 90 of them a better estimation of this parameter in the filtered spectra. In fact, in the raw spectra it was very exceptional to obtain a good result. With the filtered spectra a mean rotational splitting of $\langle\delta\nu\rangle = 4.05 \pm 0.30\text{ }\mu\text{Hz}$ was found, which is very close to the actual splitting included in the ideal spectra $\langle\delta\nu\rangle = 4.0\text{ }\mu\text{Hz}$. In addition, specific methods can be applied to improve the extraction of these parameters by using different strategies of spectra fitting as the ones developed by Gizon & Solanki (2003) or Ballot et al. (2006). In the case of the 30-day observations, the

curvelet filtered echelle diagram is still very noisy and it does not help in recognizing the ridges. However the corresponding denoised power spectrum is much better despite the lower resolution (5 times less than in the long runs), even for small S/N ratios (~ 5). The modes $\ell = 0, 2$ and $\ell = 1$ can be distinguished, at the maximum power, while it is not obvious to do so in the raw spectra. Therefore, we consider that a 30-day run is the minimum length needed to have reliable results with the curvelet denoising technique.

García et al. (2006) analyzed the first available MOST public Procyon A data (32-day observation) using the curvelet technique. Previous analysis by Matthews et al. (2004) did not reveal the presence of any p-mode structure in this star. Therefore, due to its tiny S/N ratio the results of the curvelet denoising should be taken with care. Nevertheless, an excess of power seems to appear in the region where it is expected and taking the 15 most prominent peaks in this region, many are in agreement, inside the error bars, with previous tagged modes using ground-based velocity observations.

5.2. Extraction of p-mode parameters

Once the mode identification and tagging are done, the extraction of the mode parameters can be performed. To illustrate how this extraction can be improved by using the denoised spectrum we have extracted the central frequency of the modes in both the raw and the filtered spectra. To determine this parameter, modes have been fitted by Lorentzian profiles using a maximum-likelihood estimator in the classical way: adjacent pairs of even ($\ell = 0$ and $\ell = 2$) modes are fitted together, while $\ell = 1$ is fitted alone, due to the small amplitudes of $\ell = 3$ modes. For each multiplet, the fitted parameters are the central frequency $\tilde{\nu}_{n,\ell}$, the amplitude $\tilde{A}_{n,\ell}$, the linewidth $\tilde{\Gamma}_{n,\ell}$ and the background b . The amplitude ratios inside the multiplets and the rotational splittings have been fixed thanks to the preliminary estimation done in the previous section (cf. 5.1). The fitting procedure provides for each adjusted parameter \tilde{X} an associated error $\sigma(\tilde{X})$ computed by Hessian-matrix inversion.

The raw spectra follow a χ^2 with 2 d.o.f. statistics, whereas the filtered spectra have a χ^2 with a higher d.o.f. statistics (close to a Gaussian distribution depending on the number of filtered coefficients). According to Appourchaux (2003), it is possible to fit spectra following a χ^2 with more than 2 d.o.f. statistics with a classical procedure developed for a χ^2 with 2 d.o.f. statistics: parameters are correctly fitted, but computed errors have to be adapted *a posteriori*. However in our case, due to filtering, points of filtered spectra are correlated (we have estimated that one point is correlated with ~ 10 neighbouring points). This correlation should have to be considered, but we have neglected its effect on the fitting procedure in the present study. This assumption is validated by the Monte Carlo simulations. Such a global filtering induces also correlations between the different lines of the echelle diagram. Thus the errors on parameters of different modes (typically (n, ℓ) and $(n + 1, \ell)$) can be correlated. These correlations will have to be taken into account especially during the comparison of frequencies extracted by this way to stellar models.

From the 500 realizations of the Monte Carlo simulation, we derived for each mode and for both the raw and the filtered spectra the mean value of the extracted frequencies $\langle \tilde{\nu}_{n,\ell} \rangle$, their mean computed errors $\langle \sigma(\tilde{\nu}_{n,\ell}) \rangle$ and the dispersion of frequency distribution $\sigma^*(\tilde{\nu}_{n,\ell})$ (the real error). We have verified that $\sigma^*(\tilde{\nu}_{n,\ell}) \approx \langle \sigma(\tilde{\nu}_{n,\ell}) \rangle$ for fits performed on the raw spectra and we have $\sigma^*(\tilde{\nu}_{n,\ell}) < \langle \sigma(\tilde{\nu}_{n,\ell}) \rangle$ for fits performed on the filtered ones. As expected, the error bars on the fitted frequencies, computed by Hessian-matrix inversion, are overestimated.

Figure 6 shows the difference between the mean fitted frequencies $\langle \tilde{\nu}_{n,\ell} \rangle$ and the theoretical frequencies ν_{in} of the simulated star discussed in the previous section ($S/N = 5$). The error bars correspond to the dispersion $\sigma^*(\tilde{\nu}_{n,\ell})$. For each ℓ , the error bars of the filtered spectra are smaller than those of the raw spectra. In addition, the range where modes can be detected, tagged and fitted is extended. While the difference $\langle \tilde{\nu}_{n,\ell} \rangle - \nu_{in}$ is only flat in the central region of the raw power spectrum (e.g. for $\ell = 0$, in the range $n = 18-22$), it extends at higher and lower frequencies (e.g. for $\ell = 0$, the range is extended to $n = 16-23$) in the filtered one.

6. Conclusions

The application of a noise reduction technique based on the curvelet transform to echelle diagrams improves the identification – “peak tagging” – of stellar acoustic modes. In observations with a S/N ratio as small as 5 we are still able to recover the mode pattern and extract reliable asteroseismic information in both small and long runs (30-day and 150-day observations respectively). Below this S/N and with shorter observations, the method efficiency is reduced drastically. The rotational splittings and the rotation-axis inclination can be better estimated using the filtered spectrum. In particular, Monte Carlo simulations showed that a better extraction of the mean rotational splitting from modes at low frequency can be done in 90 out of 100 realizations using the filtered spectra. The uncertainty on the extracted rotational splitting of a typical sun-like star seen with an inclination angle $i = 50^\circ$ and with a rotation $\Omega = 10\Omega_\odot$ is very small, $\sim 0.30 \mu\text{Hz}$. These parameters can then be used to have a set of guesses or *a priori* values to perform individual fits of the spectra. We have also shown that the range of the frequency extraction can be extended at higher and lower frequencies using the filtered spectra. Finally, simulations of the short run observations have demonstrated that this method can also be applied to lower resolution spectra with good results.

Acknowledgements. P. Lambert thanks Dr. D. Neuman for useful discussions.

References

- Anderson, E. R., Duvall, T. L., & Jefferies, S. M. 1990, ApJ, 364, 699
- Appourchaux, T. 2003, A&A, 412, 903
- Baglin, A., Auvergne, M., Catala, C., Michel, E., & COROT Team. 2001, in ESA SP-464: SOHO 10/GONG 2000 Workshop: Helio- and Asteroseismology at the Dawn of the Millennium, 395

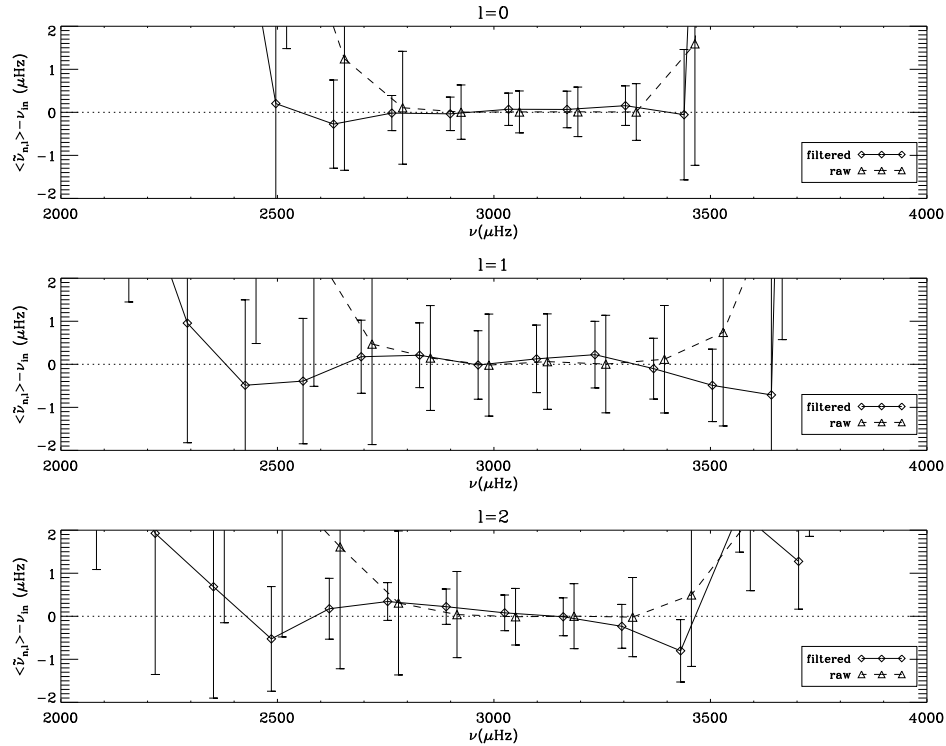


Fig. 6. Differences between the mean fitted frequencies $\langle \tilde{\nu}_{n,\ell} \rangle$ and the input frequencies ν_{in} , for $\ell = 0, 1, 2$, for the raw (dashed line with triangles) and filtered (full line with diamonds) spectra ($S/N = 5$, 150-day observation). The error bars correspond to the dispersion $\sigma^*(\tilde{\nu}_{n,\ell})$ of the frequency distribution. For clarity the values for the raw case are shifted by 20 μHz towards the right.

- Ballot, J., García, R. A., & Lambert, P. 2006, MNRAS, accepted
- Ballot, J., García, R. A., Lambert, P., & Teste, A. 2004a, in ESA SP-559: SOHO 14 Helio- and Asteroseismology: Towards a Golden Future, 309
- Ballot, J., Turck-Chièze, S., & García, R. A. 2004b, A&A, 423, 1051
- Basu, S., Mazumdar, A., Antia, H. M., & Demarque, P. 2004, MNRAS, 350, 277
- Bedding, T. R., & Kjeldsen, H. 2003, Publications of the Astronomical Society of Australia, 20, 203
- Bedding, T. R., Kjeldsen, H., Butler, R. P., et al. 2004, ApJ, 614, 380
- Bouchy, F., & Carrier, F. 2003, Ap&SS, 284, 21
- Buzasi, D., Catanzarite, J., Laher, R., et al. 2000, ApJ, 532, L133
- Candès, E. J. 1998, PhD thesis, Stanford University
- Candès, E. J., & Donoho, D. L. 1999, in Curves and Surfaces: Saint-Malo 1999, ed. A. Cohen, C. Rabut, and L. Schumaker (Vanderbilt University Press, Nashville, TN)
- Christensen-Dalsgaard, J. 2002, Reviews of Modern Physics, 74, 1073
- Fierry Fraillon, D., Gelly, B., Schmider, F. X., et al. 1998, A&A, 333, 362
- García, R. A., Jiménez-Reyes, S. J., Turck-Chièze, S., Ballot, J., & Henney, C. J. 2004, in ESA SP-559: SOHO 14 Helio- and Asteroseismology: Towards a Golden Future, 436
- García, R. A., Lambert, P., Ballot, J., et al. 2006, A&A, submitted
- Gizon, L., & Solanki, S. K. 2003, ApJ, 589, 1009
- Grec, G., Fossat, E., & Pomerantz, M. A. 1983, Sol. Phys., 82, 55
- Harvey, J. 1985, in Future Missions in Solar, Heliospheric and Space Plasma Physics, 199
- Ledoux, P. 1951, ApJ, 114, 373
- Lopes, I., & Turck-Chièze, S. 1994, A&A, 290, 845
- Matthews, J. M. 1998, in Structure and Dynamics of the Interior of the Sun and Sun-like Stars SOHO 6/GONG 98 Workshop Abstract, June 1-4, 1998, Boston, Massachusetts, 395
- Matthews, J. M., Kusching, R., Guenther, D. B., et al. 2004, Nature, 430, 51
- Monteiro, M. J. P. F. G., Christensen-Dalsgaard, J., & Thompson, M. J. 2000, MNRAS, 316, 165
- Régulo, C., & Roca Cortés, T. 2002, A&A, 396, 745
- Roxburgh, I. W., & Vorontsov, S. V. 2000a, MNRAS, 317, 141
- Roxburgh, I. W., & Vorontsov, S. V. 2000b, MNRAS, 317, 151
- Starck, J. L., Aghanim, N., & Forni, O. 2004, A&A, 416, 9
- Starck, J. L., Candès, E. J., & Donoho, D. L. 2002, IEEE Transactions on Image Processing, 11, 670
- Starck, J. L., Donoho, D. L., & Candès, E. J. 2003, A&A, 398, 785
- Tassoul, M. 1980, ApJS, 43, 469
- Turck-Chièze, S., Däppen, W., Fossat, E., et al. 1993, Phys. Rep., 230, 57
- Vorontsov, S. V. 1991, Soviet Astronomy, 35, 400